RNA-dependent RNA polymerase of predominant human norovirus forms liquid-liquid phase condensates as platforms for viral replication

Soni Kaundal[1], Ramakrishnan Anish [1], B. Vijayalakshmi Ayyar[2], Sreejesh Shanker[1], Gundeep Kaur[3], Sue E. Crawford[2], Jeroen Pollet[4], Fabio Stossi[5], Mary K. Estes[2,6], B.V. Venkataram Prasad[1,2]

[1]Department of Biochemistry and Molecular Pharmacology and [2]Department of Molecular Virology and Microbiology, Baylor College of Medicine, Houston, Texas, U.S.A. [3]Department of Epigenetics and Molecular Carcinogenesis, The University of Texas, MD Anderson Cancer Center, Houston, Texas U.S.A., [4]Department of Pediatrics-Tropical Medicine, [5]Department of Molecular and Cellular Biology, and [6]Department of Medicine, Baylor College of Medicine, Houston, Texas, U.S.A.

Corresponding author: B. V. Venkataram Prasad, E-mail: vprasad@bcm.edu

Abstract

Biomolecular condensates are membrane-less cellular foci formed via liquid-liquid-phase separation (LLPS) of specific biological macromolecules to provide specialized compartments for regulating cellular functions. Many viral proteins undergo LLPS to form such condensates to support viral replication and evade host antiviral responses, and thus, these condensates are potential targets for designing antivirals. Human noroviruses (HuNoV) cause epidemic and sporadic gastroenteritis worldwide and are of significant health and economic burden. Here, we show that the RNA-dependent-RNA polymerase (RdRp) of the pandemic GII.4 HuNoV, which is essential for viral replication, forms distinct condensates capable of recruiting other viral replication components. Confocal microscopy and light scattering experiments show that RdRp phase separates into dynamic liquid-like condensates at physiological conditions. These condensates exhibit all the signature features of LLPS, including fluorescence recovery after photo-bleaching, droplet-fusion, surface wetting, and dripping in vitro and in live cells. More importantly, within these condensates, the RdRp exhibits a significant time-dependent increase in its enzymatic activity and recruits other components, such as RNA and the viral genome-linked protein (VPg), which are essential for viral replication. Such condensates, recognized by anti-RdRp antibodies, are observed in HuNoV-infected human intestinal enteroid cultures. Together, our studies demonstrate a hitherto unsuspected activity of HuNoV RdRp to form LLPS, which we suggest provides distinct cellular sites for efficient viral replication and its regulation.

42 # Introduction

43 The compartmentalization of biomolecules is essential for efficiently regulating numerous
44 biological processes in a densely packed cellular environment. A wealth of new research has
45 shown that, apart from the traditional membrane-bound organelles, eukaryotic cells also contain
46 membrane-less organelles such as P granules, nucleoli, Cajal bodies, etc. [1-7]. These membrane-less
47 organelles, also known as biomolecular condensates, are formed by the process of liquid-liquid
48 phase separation (LLPS), where a single, uniform liquid phase separates into a dense phase that
49 coexists with the surrounding dilute phase [8-13]. These condensates, often initiated by a single
50 protein, selectively allow the incorporation of proteins and nucleic acids to provide exclusive
51 compartments for performing specialized cellular functions, including gene regulation, protein
52 synthesis, and signaling [13-15]. Depending upon the sequence and concentration of the protein, the
53 presence of other biomolecules, and the physiochemical properties of the surroundings, the dense
54 phase can have material properties of liquid, gel, or solid [2,3,16,17]. The liquid-like condensates
55 typically have a spherical shape with a dynamic interior, and exhibit the ability to fuse with each
56 other, deform upon physical contact, and revert to the spherical shape [2,3,9,10]. Signature features of
57 the proteins undergoing LLPS include the presence of a nucleic acid binding domain, a disordered
58 region, a low complexity region, and the ability to form oligomers [18-21]. The intrinsically
59 disordered regions drive LLPS by weak and dynamic intermolecular contacts, including
60 hydrophobic, electrostatic, hydrogen bonding, cation-π, and π-π interactions. The dynamic making
61 and breaking of these weak interactions give rise to the liquid-like nature of the phase separated
62 condensates [18,22,23]. The lack of a physical barrier and metastable state of these condensates allows
63 the rapid exchange of their components with surrounding molecules providing a unique
64 spatiotemporal regulation of macromolecular organization and cellular biochemistry [24,25].

65 Recent studies showed that several viral proteins can induce the formation of biomolecular
66 condensates via LLPS. These include, for example, NSP5 protein of rotavirus [26], N protein of
67 SARS-CoV2 [27], N protein of HIV-1 [28], and NS2 protein of bluetongue virus [29]. These condensates
68 are suggested to provide facile compartments also called viral factories or viroplasms for
69 concentrating the necessary components for efficient viral replication and assembly [30-32]. The
70 formation of condensates by LLPS is also proposed as a mechanism for evading the host antiviral
71 response [33,34].

72 Currently, it is unknown whether any of the proteins encoded by human norovirus
73 (HuNoV) undergoes LLPS to form biomolecular condensates. HuNoVs are the leading cause of
74 viral gastroenteritis and pose a significant global health and economic burden without any
75 approved vaccines or antivirals [35,36]. These icosahedral, single-stranded RNA viruses, belonging
76 to the *Norovirus* genus in the *Caliciviridae* family account for an estimated ~685 million cases and
77 ~212,000 deaths globally per year with an economic impact of $60 billion [35-39]. The NoVs are
78 classified into at least 10 genogroups (GI-GX) and 49 genotypes [40]. NoVs in genogroups GI, GII,
79 GIV, GVIII, and GIX infect humans [40,41], and among these, HuNoVs belonging to genogroup II
80 and genotype 4 (GII.4) are responsible for ~80 % of the outbreaks worldwide [42]. The NoV genome
81 is covalently linked to VPg and consists of three open reading frames (ORFs). ORF1 encodes a
82 polyprotein that is cleaved into six nonstructural proteins by the viral protease to produce p48
83 (NS1-2), p41 (NS3), p22 (NS4), VPg (NS5), protease (NS6), and RNA-dependent RNA
84 polymerase (RdRp) (NS7) [43]. The ORF2 and ORF3 encode the major capsid protein VP1 and a
85 minor structural protein VP2, respectively [44]. Our understanding of the HuNoV replication
86 processes in infected cells has been hampered by lack of a robust cell culture system. Much of our
87 current understanding of the entry and replication processes of HuNoVs have come from using the

88 human intestinal stem cell-derived, nontransformed enteroid (HIE) monolayer cultures for virus
89 cultivation [45-47].

90 Using bioinformatics analysis, we found that among the nonstructural proteins
91 encoded by the pandemic GII.4 Sydney strain, RdRp has the highest propensity to undergo LLPS
92 to form biomolecular condensates. In addition to the biophysical proprieties of GII.4 RdRp, such
93 as its modular architecture, the presence of an N-terminal disordered region, the ability to homo-
94 oligomerize and bind RNA, and the critical role it plays during viral replication prompted us to
95 experimentally test the hypothesis that GII.4 RdRp drives the formation of biomolecular
96 condensates that are conducive for viral replication through LLPS. Our studies show that RdRp,
97 consistent with its biophysical properties, indeed forms highly dynamic liquid-like condensates
98 via LLPS at physiologically relevant conditions and that the disordered N-terminal region of GII.4
99 RdRp is critical for LLPS. HuNoV infected HIEs cells show distinct condensates recognized by
100 RdRp antibodies. We also demonstrated a time-dependent increase of the GII.4 RdRp enzymatic
101 activity in the condensates and the ability of these condensates to sequester the components of
102 viral replication factories. Together these findings establish that HuNoV RdRp undergoes LLPS
103 to form biomolecular condensates, which can serve as platforms for viral replication.

104 # Results

105 **GII.4 RdRp exhibits the obligatory properties to undergo LLPS**

106 We used the DeePhase server [48] to analyze the primary amino acid sequences of all the
107 nonstructural proteins encoded by HuNoV GII.4 (Sydney) for their ability to undergo LLPS (**Fig.**
108 **1a**). This analysis predicted that RdRp, with an overall score of 0.67, has the highest propensity
109 to undergo LLPS. The known biochemical and enzymatic properties of RdRp are consistent with
110 this prediction. As a protein critical for the transcription and replication of genomic RNA, the

111 RNA binding property of RdRp satisfies one of the essential criteria for undergoing LLPS. Another
112 requirement is the presence of disordered regions. Analysis by PONDR (**Fig. 1b**) [49] and IUPred2
113 (**Fig. 1c**) [50] software shows the presence of disordered N- terminal ~50 residues in RdRp, which is
114 consistent with the currently available crystal structures of NoV RdRps [51-54].

115 To experimentally confirm the LLPS driving properties of RdRp, such as the presence of
116 a disordered region and the ability to form oligomers, we purified recombinantly expressed GII.4
117 RdRp and determined its X-ray crystal structure at 2.0 Å resolution using molecular replacement
118 (PDB ID: 8TUF). The crystal structure shows, as expected, all the features observed in the previous
119 crystallographic structures of the NoV RdRps [51-54], including the disordered N-terminal tail of 50
120 residues. The polypeptide fold resembles a partially closed right hand, with fingers, thumb, and
121 palm as subdomains (**Fig. 1d, Supplementary Table 1**). Size exclusion chromatography (SEC)
122 (**Fig. 1e**) and sedimentation velocity analytical ultracentrifugation (SV-AUC) (**Fig. 1f**) of the
123 recombinant RdRp show that while most of the RdRp (75 %) exists as a monomer in
124 physiologically relevant conditions, a fraction of which also tends to form dimers (15 %) and
125 higher-order oligomers. These experimental data, consistent with the bioinformatic predictions,
126 suggest that RdRp is a suitable candidate to investigate further its phase separation behavior.

127 **GII.4 RdRp undergoes phase separation to form dynamic liquid-like condensates**

128 To experimentally validate that RdRp undergoes LLPS, we studied its phase separation
129 behavior in vitro using light scattering experiments and confocal microscopy. Under physiological
130 conditions, homogeneously mixed RdRp (10 μM) phase separates to form a demixed turbid
131 solution when incubated at 37 °C for 45 min (**Fig. 2a**). The presence of condensates in the phase
132 separated solution was examined by confocal microscopy using a mixture of Atto 488-labeled (1
133 %) and unlabeled (99 %) RdRp. The micrographs showed the formation of spherical condensates
134 of micron diameter (**Fig. 2b**). We examined the liquid-like nature of these condensates by

135 assessing fluorescence recovery after photobleaching (FRAP) of the RdRp molecules. In this
136 experiment, the condensate was photo-bleached by intense laser light in a confocal microscope,
137 and then the fluorescence recovery of the photo-bleached area was monitored over time. The rapid
138 fluorescence recovery indicates diffusion of RdRp molecules. The FRAP data revealed a complete
139 fluorescence recovery (98 %) with a half-life ($t_{1/2}$) of 53.3 ± 2.1 s (**Fig. 2c, d**). Using time-lapse
140 confocal microscopy, we observed smaller GII.4 RdRp condensates fuse to form a larger
141 condensate (**Fig. 2e**). These condensates also undergo surface wetting and dripping (**Fig. 2f**). These
142 are also signature properties of liquid condensates. Our results clearly show that GII.4 RdRp
143 undergoes phase separation to form dynamic, liquid-like condensates, which are dense and high in
144 RdRp concentration yet allow the RdRp molecules to move freely within the condensates and
145 exchange with the surrounding environment.

146 **Molecular crowding, pH and salt concentration modulate phase separation properties of**
147 **GII.4 RdRp**

148 To examine whether there is a critical concentration of RdRp necessary to undergo LLPS,
149 and how this concentration is affected by molecular crowding agents such as polyethylene glycol
150 (PEG), typically used to simulate intracellular molecular crowding, we used two different
151 techniques: light scattering experiments to measure turbidity (**Fig. 3a**) and confocal microscopy to
152 assess LLPS formation (**Fig. 3d**). Different concentrations (0.5-25 μM) of GII.4 RdRp were
153 screened with and without PEG3350 (5-20 %). Confocal microscopy results suggest the critical
154 concentration for phase separation of GII.4 RdRp decreases from 5 μM to 0.5 μM by adding 10 %
155 PEG3350. The results show that increasing the molecular crowding, as expected inside the cells
156 during virus replication, decreases the critical concentration of the protein to phase separate. Our
157 light scattering experiments with PEG3350 also supported this result.

158 Considering the possibility, as observed in several recent studies [55,56,57,58], that changes in
159 intracellular pH and salt concentrations profoundly influence viral replication, we examined if
160 these factors affect the phase separation behavior of GII.4 RdRp. We observed increased turbidity
161 at an acidic pH of 5.5 compared to neutral pH, indicating that acidic pH promotes phase separation
162 more effectively than neutral pH. In contrast, the turbidity was significantly less at an alkaline pH
163 of 9.0 **(Fig. 3b)**. Since turbidity measurement is affected by the condensates size, shape, and
164 density, we further performed confocal microscopy at different pH conditions (**Fig. 3e**). RdRp
165 forms larger condensates at pH 5.5 than at pH 7.5 and, at pH 9, the condensates are few and have
166 an irregular shape. In addition, at pH 5.5, the critical concentration of RdRp required to form
167 LLPS decreased to 0.5 μM from 5 μM at pH 7.5. Since the predicted pI of GII.4 RdRp is 6.16,
168 these observations suggest that positive charges from basic residues in RdRp are critical for
169 promoting phase separation.

170 We also tested the effect of ionic strength on the phase separation of GII.4 RdRp by
171 measuring the turbidity of the solutions containing varying concentrations of NaCl using turbidity
172 measurements at 350 nm **(Fig. 3c),** and by imaging the condensates using confocal microscopy
173 **(Fig. 3f)**. These studies showed GII.4 RdRp undergoes phase separation at a NaCl concentration
174 as low as 10 mM, but not at concentrations >500 mM. The low ionic strength enhances protein-
175 protein electrostatic or π-π interactions, whereas high salt abolishes these interactions. Recent
176 studies have shown a similar behavior of the N protein of SARS-CoV-2 concerning pH and ionic
177 strength [28].

178 **The disordered N-terminal region is critical for GII.4 RdRp LLPS**

179 To validate the predicted role of the disordered N-terminal region of RdRp in forming the
180 condensates, we expressed and purified two N-terminal deletion constructs, GII.4 RdRp-NΔ13 and
181 GII.4 RdRp-NΔ51. Size exclusion chromatography of both deletion constructs shows a reduction

182 in their ability to form oligomers **(Fig. 4a)**. The CD spectra of both these constructs, showed two
183 distinct negative maxima at λ = 208 nm and 220 nm and a strong positive peak around 190 nm
184 indicative of an α-helical conformation and thus of proper folding of the deletion constructs **(Fig.**
185 **4b)**. Confocal microscopy images show that while GII.4 RdRp-NΔ13 can form liquid condensates
186 **(Fig. 4c)**, with a distorted and not spherical shape as compared with the full-length RdRp. The
187 distorted shape may be due to the weakened interactions resulting from the deletion of 13 residues,
188 which contain one aromatic residue. In contrast, deletion of N-terminal 51 residues (GII.4 RdRp-
189 NΔ51), which includes 5 aromatic residues, showed few and very small condensates that were
190 difficult to image. Our studies thus clearly demonstrate the flexible N-terminal region of GII.4
191 RdRp plays a critical role in its phase separation behavior.

192 **GII.4 infected HIE cells show phase separated RdRp condensates**

193 To investigate if RdRp condensate formation occurs in the context of viral replication, we
194 infected HIEs with GII.4 HuNoV and imaged the cells using confocal microscopy at different time
195 points post-infection. The confocal images show the presence of discrete and spherical condensates
196 of RdRp (detected by anti-RdRp antibody) **(Fig. 5a)**, which gradually increase in size over time.
197 We could not perform the FRAP/fusion experiments, in these virus-infected cells as these samples
198 needed to be fixed with paraformaldehyde and permeabilized for immunolabeling. In lieu of this,
199 we investigated if a recombinant GII.4 RdRp-eGFP forms condensates with liquid-like properties
200 upon transfection in HEK293T cells. Confocal microscopy imaging of the live cells 24h post-
201 transfection showed round condensates formed by RdRp (**Fig. 5b)**. In contrast, cells expressing
202 eGFP alone, as a negative control, exhibit a diffuse distribution of eGFP (**Fig. 5b**). The condensates
203 formed by RdRp-eGFP show recovery after photo-bleaching indicating their liquid-like nature
204 **(Fig. 5b and c)**. Together, these findings provide supporting evidence that the observed
205 condensates in the virus-infected HIEs cells are formed via LLPS driven by RdRp.

206 **GII.4 RdRp is enzymatically active within liquid condensates**

207 Before investigating whether RdRp is active within the condensates, we used the
208 centrifugation method to estimate the concentration of phase separated RdRp, which was ~2.2
209 mM, ~200 times higher than the surrounding dilute phase, measured at A_{280}. To examine if the
210 highly concentrated protein in the condensate is enzymatically active, we monitored the formation
211 of dsRNA from a ssRNA template using a well-established fluorescence-based assay in which the
212 fluorescent dye SYTO9 binds specifically to dsRNA and fluoresces when excited at 485 nm **(Fig.**
213 **6a)**. We started the RNA polymerization reaction by adding rGTP (substrate) to a mixture which
214 includes RdRp (enzyme), polyC (ssRNA template), SYTO9 dye and other reaction components.
215 The reaction was performed in a 96 well glass bottom plate at 37 °C and imaged every 20 min
216 using a Yokogawa CV8000 high throughput spinning disk confocal microscope. Analysis of time-
217 lapse images shows an increase in fluorescence intensity within the condensates over time,
218 suggesting the formation of dsRNA **(Fig. 6b)**. An increase in the fluorescence intensity was
219 observed on the analysis of the total fluorescence intensity using CellPathfinder software **(Fig. 6c)**.
220 Together these results show concentration- and time-dependent increase in the enzymatic activity
221 of RdRp within the condensates.

222 **GII.4 RdRp LLPS recruits the critical components of viral replication machinery**

223 After demonstrating that RdRp can undergo LLPS to form enzymatically active
224 biomolecular condensates, we investigated whether these condensates could sequester the critical
225 components of the viral replication machinery, such as RNA and VPg, which functions as a primer
226 to initiate replication [59,60]. To examine the incorporation of RNA into the condensates, we mixed
227 equimolar amounts of Atto-488 RdRp andCy5 labeled RNA and imaged the samples using
228 confocal microscopy. Confocal microscopy revealed colocalization of Cy5-RNA and Atto 488-
229 RdRp condensates (**Fig. 7a**). Next, we tested if RdRp condensates can recruit GII.4 VPg. We

230 generated a reaction mixture by mixing equimolar amounts of Atto-488 RdRp and Atto-647N VPg
231 that were analyzed by confocal microscopy. We observed co-localization of VPg in the GII.4
232 RdRp condensates (**Fig. 7b**). The same results were obtained in HEK293T cells upon the
233 transfection of RdRp-eGFP and mCherry-VPg (**Fig. 7c**), where we could also observe the fusion
234 of these condensates (**Fig. 7d**). These results suggest that GII.4 RdRp phase separation offers a
235 mechanism for bringing together components of the viral replication machinery.

236 **Liquid to solid transition of GII.4 RdRp triggers the formation of amyloid-like fibrils.**

237 To study the dynamics of protein molecules during the maturation of the GII.4 RdRp
238 condensates, we monitored the material properties of the condensates for 24h using FRAP. In
239 initial experiments, the FRAP data revealed a complete fluorescence recovery (98 %) with a half-
240 life ($t_{1/2}$) of 53.3 ± 2.1 s, which decreased significantly with time (**Fig. 8a and b**). These
241 condensates retained liquid-like properties for about 4 h and then transformed into gel-like or solid-
242 like condensates. The increased rigidity and reduced dynamicity of protein molecules within the
243 condensates suggest that, over time, these condensates change from liquid-like to solid-like, likely
244 driven by the aggregation of proteins. Negative staining transmission electron microscopy of the
245 phase separated samples after 12 h of incubation at 37 °C showed fibrillar structures of varying
246 lengths **(Fig. 8c)**. Surprisingly, these fibrils have amyloid-like characteristics, such as binding to
247 amyloid-specific dyes thioflavin T (ThT) **(Fig. 8d)** and Congo red (CR) **(Fig. 8e)**. Such a
248 transformation from liquid-like to solid-like amyloid fibrils might provide a mechanism to regulate
249 viral replication.

250

251 # Discussion

252 In recent years, in addition to their demonstrated role in regulating various cellular
253 functions, biomolecular condensates formed via LLPS are strongly implicated in forming viral
254 replication factories/inclusion bodies [26,30,32]. For example, the viroplasms formed during rotavirus
255 infection, the sites for genome replication and sub-particle assembly, are considered biomolecular
256 condensates formed by the nonstructural proteins NSP5 and NSP2 [26]. In the case of SARS-CoV-
257 2, the N protein undergoes LLPS and sequesters components of the viral replication machinery [32].
258 Although replication factories (RFs) for HuNoVs are not yet characterized, murine NoVs form
259 distinct RFs [61]; however, the involvement of LLPS in these RFs is yet to be explored. In this
260 study, we show that RdRp of GII.4 HuNoV undergoes phase separation under physiologically
261 relevant conditions to create liquid-like, dynamic condensates that contain a protein-rich, dense,
262 and highly mobile environment. Our studies further suggest that distinct puncta observed in GII.4-
263 infected HIEs, which are recognized by anti-RdRp antibodies, are similar to the liquid-like
264 condensates formed by RdRp in HEK293T cells. We posit that these puncta are RdRp-initiated
265 liquid-like condensates representing RFs. Bioinformatics analysis shows that RdRps of almost all
266 the norovirus genogroups have a high propensity to form LLPS (**Supplementary Fig. 1**),
267 suggesting that LLPS formation by RdRp may be a common phenomenon in the Norovirus genera.
268 Although LLPS formed by cellular [62] and bacterial polymerases [63] is known, this is the first report
269 of a viral RdRp undergoing LLPS under physiological conditions both in vitro and in vivo.

270 **Unique aspects of HuNoV GII.4 RdRp induced LLPS – initiating a hub for viral replication**

271 Typically, cellular or viral proteins require additional client proteins, crowding agents, or
272 RNA to phase separate under physiological conditions [(35, 40)]. For example, up to 50 μM of the
273 SARS-CoV-2 N protein does not phase separate but adding 1 μM poly U significantly promotes
274 the phase separation [(40)]. Similarly, 35 μM NSP5 of rotavirus does not phase separate by itself; but
275 requires the presence of NSP2 or poly-arginine for phase separation [(35)]. In contrast, GII.4 RdRp

276 does not require any other viral protein or RNA to phase separate. It can phase separate at 5 μM
277 by itself and at 500 nM by adding a molecular crowding agent. Another observation, which may
278 have implications for viral replication, is that RdRp undergoes LLPS at pHs ranging from 5 to 9.
279 Interestingly, at pH 5, the critical concentration of RdRp to form LLPS is reduced from 5 μM to
280 500 nM. This is consistent with the previous observations that GII.4 and GII.3 HuNoVs infection
281 induces endosomal acidification [45,64]. The ability of GII.4 RdRp to readily form LLPS on its own
282 under various concentrations and conditions suggests that it likely plays a role in initiating the
283 formation of a sustainable platform for efficient viral replication during infection.

284 **RdRp condensates as viral replication factories**

285 A critical aspect of biomolecular condensates formed via LLPS, which is relevant for
286 forming viral RFs, is that they concentrate protein, nucleic acid, and other biomolecules to increase
287 and regulate reaction rates. In our studies, we observed not only that the concentration of phase
288 separated RdRp is ~200 times greater than that in the dilute phase but also that RdRp is
289 enzymatically active in such a crowded environment, supporting the hypothesis that these
290 condensates could be sites for viral replication. The observation that these RdRp condensates
291 promote the cooperative association/sequestering of other important viral components of the viral
292 replication machinery, such as RNA and VPg, further supports these condensates as platforms for
293 viral replication. VPg is a critical protein involved in viral replication and translation of viral
294 proteins. A recent study on murine NoV suggested that apart from its priming function, VPg can
295 physically interact with RdRp and enhance its polymerization activity [52]. Our results on HuNoV
296 RdRp also suggest that VPg increases the polymerization activity of RdRp (unpublished data).
297 Similarly, it is reported that the condensates formed by the N protein of SARS-CoV-2 can
298 sequester RNA and RdRp to provide a platform for viral replication [65]. Also a recent report suggest
299 the presence of RdRp in the Ebola virus VFs which are biomolecular condensates [66].

300 Another protein that possibly is a component of the viral replication factory is p41 (NS3),
301 a membrane-anchored protein with RNA helicase activity [67]. p41 may be recruited into the RdRp
302 condensates containing VPg and RNA either by passive diffusion or by interacting with viral RNA.
303 Although not unequivocally demonstrated, earlier studies on picornaviruses, murine noroviruses,
304 and other positive sense RNA viruses have suggested that replication factories are associated with
305 membranes [61,68,69,70]. The formation of LLPS as a potential hub or a driving force for forming the
306 replication factories does not exclude the incorporation or association of membrane-anchored
307 proteins and lipids. Recent studies have implied such an association could reduce the critical
308 concentration for inducing LLPS and further for forming microdomains within the membrane-
309 associated condensates [71,72].

310 **Liquid to solid transition as a regulatory mechanism**

311 Another common phenomenon of biomolecular condensates is the transition from a liquid
312 to a solid state over time. The FRAP analysis of the GII.4 RdRp condensates over time shows a
313 lower diffusion rate of the RdRp molecules in the condensates. Consistent with this observation,
314 TEM imaging of the RdRp incubated at 37 °C overnight demonstrated the formation of fibrils.
315 Interestingly, these fibrils bind to amyloid-specific dyes such as ThT and CR, indicating the
316 amyloid-like nature of these fibrils. RdRps of several picornaviruses also form similar fibrillar
317 structures [73-75], although whether they exhibit amyloid-like properties is still unknown. The
318 transition from liquid to solid state leading to the formation of amyloid-like fibrils is plausibly a
319 mechanism for regulating replication. Another possibility is that these amyloid-like fibrils may
320 have a role in inducing cell toxicity, as shown in the case of amyloid-like fibrils formed by the
321 NS11 protein of SARS-CoV-2 [76].

322 In summary, our study reveals a previously unknown property of HuNoV RdRp in forming
323 biomolecular condensates. In addition to exhibiting all the properties for inducing the formation

324 of LLPS in vitro, we have shown that RdRp also readily undergoes LLPS in a cellular environment
325 that resembles the condensates observed in virus infected HIEs strongly implicating RdRp in
326 initiating and sustaining the viral RFs during HuNoV infection. Our bioinformatics analysis
327 suggests that this indeed may be a common phenomenon in most noroviruses. The implication of
328 RdRp in forming RFs also opens new targets for designing antivirals for HuNoV infections, which
329 remains a serious threat in children and immunocompromised patients.

330

331 # Material and methods

332 **Cloning, expression, and purification of proteins**

333 Codon optimized RdRp and VPg genes of HuNoV GII.4 Sydney strain (GenBank: AFV08794.1)
334 were synthesized and cloned in the pET28a vector for bacterial expression by Genscript U.S.A.
335 Inc with an N-terminal 6x His-tag to aid in the purification of both proteins. For mammalian
336 expression GII.4 RdRp was cloned in pcDNA3.1(+) vector with eGFP on C-terminal and GII.4
337 VPg was cloned in pcDNA3.1(+) vector with mCherry on N-terminal by Genscript U.S.A. Inc.
338 Two N-terminal truncations, i.e., GII.4 RdRp-NΔ13 and GII.4 RdRp-NΔ51 were also generated
339 by Genscript U.S.A. Inc. For the over-expression of proteins, the plasmids containing the desired
340 genes were transformed into *E coli* BL21 (DE3) cells. Protein expression was induced by addition
341 of 0.3 mM isopropyl β-D-1-thiogalactopyranoside at OD_{600} ~0.6. Cells were allowed to express
342 the protein at 18 °C for 16h with constant shaking at 200 rpm. Cells were harvested by
343 centrifugation at 4000xg for 30 min at 4 °C and the pellet was re-suspended in lysis buffer (20 mM
344 Tris-HCl pH 7.5, 250 mM NaCl, 5 mM imidazole and a cocktail of protease inhibitors) followed
345 by cell disruption using a microfluidizer. The supernatant was collected after centrifugation at
346 18,000xg for 45 min at 4 °C. The protein was purified by affinity chromatography using Ni-NTA

347 agarose (Qiagen) resin followed by gel filtration using Superdex 200 Increase 10/300 GL column
348 (G.E. Healthcare) in 20 mM Tris-HCl pH 7.5, 150 mM NaCl and 5 mM DTT. All the target
349 proteins GII.4 RdRp, GII.4 RdRp-NΔ13, GII.4 RdRp-NΔ51, and GII.4 VPg were purified using
350 the above-mentioned protocol to a purity of >95% as judged by SDS-PAGE and Coomassie blue
351 stain.

352 **Analytical ultracentrifugation**

353 To study the oligomeric state of GII.4 RdRp, sedimentation velocity experiments of 10 μM GII.4
354 RdRp were carried out using a Beckman-Coulter XL-A analytical ultracentrifuge with a TiAn60
355 four-hole rotor and two-channel epon centerpieces (12 mm) at 40,000 rpm at 22 °C. Absorbance
356 scans were recorded at 280 nm at 1 min intervals. A continuous distribution c(s) model was used
357 to fit multiple scans at regular intervals with SEDFIT [77]. The solvent density (ρ) and viscosity (
358 η) were calculated from the chemical composition of different proteins by SEDNTERP [78].

359 **Protein crystallization**

360 Crystallization screenings for GII.4 RdRp (10 mg/ml)was carried out by hanging-drop vapor
361 diffusion using the Mosquito crystallization robot (TTP LabTech) and imaged using Rock Imager
362 (Formulatrix) at 20 °C. The protein was crystallized under the condition 0.3 M Sodium Iodide, 0.1
363 M Sodium Acetate: HCl, pH 4.5 22.5 % (v/v) PurePEGs Cocktail. Crystals were flash-frozen
364 directly in liquid nitrogen.

365 **Structure determination and refinement**

366 X-ray Diffraction data for GII.4 RdRp was collected on APS beamline17-ID. Diffraction data were
367 processed with IMOSFLM as implemented in the CCP4 suite [79]. The structure of NV RdRP (PDB
368 ID: 4LQ3) was used as a search model for molecular replacement (MR) using PHASER. The
369 atomic model including the side chain atoms was then subjected to iterative cycles of refinement

370 using PHENIX and further model building using COOT based on the difference maps [80,81]. Data
371 collection and refinement statistics following final refinement cycle are given in Supplementary
372 Table 1.

373 **Light scattering measurements**

374 Light scattering measurements of GII.4 RdRp were carried out on a FlexStation3 plate reader
375 (Molecular devices) using a 96-well flat bottom plate (Fisher Scientific) by measuring absorbance
376 at 350 nm at 37 °C at a regular interval of 2 min. Different concentrations of GII.4 RdRp (0.5, 1,
377 5, 10, 25 μM) were screened at varying concentrations of PEG3350 (0, 5, 10, 20%), pH (5.0, 6.0,
378 7.5, and 9.0) and salt (NaCl) (0, 150, 300, 500, and 750 mM).

379 **Fluorescence labeling of proteins**

380 For microscopic visualization of condensates, GII.4 RdRp, GII.4 RdRp-NΔ13 and GII.4 RdRp-
381 NΔ51were labeled with Atto-488 and GII.4 VPg was labeled with Atto-647N dye. For labeling an
382 Atto 488 protein labeling kit (Sigma-Aldrich, 38371) and an Atto 647N protein labeling kit
383 (Sigma-Aldrich, 76508) were used. The manufacture's provided protocol was used. Briefly, 8
384 mg/ml RdRp, RdRp-NΔ13, RdRp-NΔ51, and 6 mg/ml VPg were dialyzed in sodium bicarbonate
385 buffer solution, pH 9.5 (provided with kit). Then the protein solution was transferred to a vial
386 containing the reactive dye dissolved in 20 μl sodium bicarbonate buffer and incubated the reaction
387 mixture for 2 h at room temperature while gently stirring and protecting the vial from light. For
388 separation of protein-dye-conjugates from free dye, manufacturer's provided gel filtration columns
389 were used to achieve good separation of the protein-dye-conjugates from excess free dye (size
390 exclusion limit: 5 kDa). The protein-dye-conjugates were eluted in phosphate buffer, pH 7.5
391 provided with the kit.

392 **Confocal microscopy**

393 Protein mixtures of 1% labeled and 99% unlabeled proteins were made at a concentration of 10
394 μM. An aliquot (15 μl) of the protein mixture was spotted onto 15 mm depression slides and
395 sandwiched with an 18 mm coverslip followed by sealing of the edges of the coverslip with
396 commercially available nail polish and allowed to phase separate at 37 °C for 45 min. The
397 condensates were visualized by Nikon A1R-s confocal microscope with 40X- air objective and 1
398 Airy unit aperture.

399 Different concentration of GII.4 RdRp (0.5, 1, 5, 10, 25 μM) were screened at varying
400 concentration of PEG3350 (0, 5, 10, 20 %), pH (5.0, 6.0, 7.5, and 9.0) and salt (NaCl) concentration
401 (0, 150, 300, 500, and 750 mM using Yokogawa CV8000 confocal imaging platform.

402 **Far-UV circular dichroism (CD) measurements**

403 Far-UV CD measurements of RdRp, RdRp-NΔ13, and RdRp-NΔ51 were carried out using
404 Circular Dichroism Spectroscopy (J-1500, Jasco), using a 1-mm path-length quartz cuvette. Data
405 were recorded using a final protein concentration of 8 μM proteins in 20 mM sodium phosphate
406 buffer pH 7.5. The spectra were averaged over three scans and were blank subtracted. The spectra
407 were then processed using Spectra Manager™ CDPro (Jasco) and plotted using Origin 2018.

408 **Negative-stain transmission electron microscopy (EM)**

409 GII.4 RdRp (10 μM, 50 ul) was incubated at 37 °C at a constant shaking at 200 rpm for 20 s after
410 every 2 min for a period of 12 h. For preparing negatively stained grids, 3 μl of the GII.4 RdRp
411 (diluted 10 times) was adsorbed onto a glow discharged grid carbon-coated grid (CF200-CU;
412 EMS) for 60 s. The grid was blotted with Whatman's filter paper 541 and washed twice with
413 deionized water with intermittent blotting. The grid was further stained with three drops of 2 %
414 uranyl acetate with intermittent blotting to remove the residual stain. The grids were air-dried and
415 imaged at room temperature using a JEM 2100 transmission electron microscope operated at 200
416 keV (JEOL) equipped with a LaB6 filament, 3kx4k Direct Electron Detector (DE12) and a Gatan

417 4kx4k CCD at the cryo-EM core facility, Baylor college of Medicine. The images were recorded
418 at 15k using a low-dose procedure and a defocus range of −1 to −4 μm.

419 **GII.4 HuNoV infection of HIE monolayers**

420 Five day differentiated monolayers were infected with 1 x 10^7 GE of GII.4 stool filtrate in
421 CMGF(-) for 1 h at 37 ºC. After washing two times with CMGF(-), the HIEs were incubated at 37
422 °C for different time points (8-20 h). The cells were fixed with 4% paraformaldehyde (PFA) for
423 20 min at room temperature followed by permeabilization with 0.1% Triton X-100 (for
424 permeabilization) in PBS for 30 min at room temperature. The cells were incubated with 1:150
425 dilution of rabbit anti-RdRp [82] in 5 % BSA PBS at 4 °C overnight. The cells were washed three
426 times with PBS containing 0.1 % Triton X-100 and incubated with goat anti-rabbit 488 (#A-11008,
427 ThermoFisher Scientific) overnight at 4 º C to visualize the viral proteins. The cells were washed
428 three times, and the nuclei were stained with 4, 6-diamidino-2-phenylindole (DAPI) (300 nM)
429 followed by subsequent Z-stack images captured using a Nikon A1 confocal microscope.

430 **Mammalian cell line and expression**

431 HEK293T (ATCC, CRL-3216) (2 x 10^5 cells per well) were seeded in μ-Slide 8-well glass-bottom
432 plates (Ibidi) in DMEM media and incubated at 37 °C for 24 h. Cells were then transfected with
433 respective plasmids and incubated 37 °C. After 24 h, the cells were stained with Hoechst 33342
434 diluted in FluoroBRITE DMEM at a concentration of 1 mg/mL, incubated for 30 min at 37 °C.
435 These cells were further used for confocal microscopy and FRAP experiments.

436 **Fluorescence recovery after photobleaching (FRAP)**

437 FRAP studies were performed using a laser scanning confocal microscope (Nicon-A1R-s) with a
438 40x air objective. A circular area encompassing an entire condensate was bleached with a 404 nm
439 laser (100 %) for 20 iterations and recovery was recorded for 300 s at 10 s intervals. For in vitro

440 FRAP study, 15 µl RdRp (10 µM) was spotted onto 15 mm depression slides and sandwiched with
441 18 mm coverslip followed by sealing of the edges of the coverslip with commercially available
442 nail polish and allowed to phase separate at 37 °C. After droplet formation was confirmed, the
443 slides containing the condensates were subjected to FRAP experiments at various time points as
444 indicated in the respective sections. For live cell FRAP, the bleaching of ROI was performed at 70
445 % laser power for 20 iterations and recovery was recorded for 500 s at 15 s interval. The images
446 were corrected for laser bleaching by selecting a fluorescent region outside the ROI.

447 **Estimation of light phase and dense phase concentration**

448 The concentrations of dense phase and light phase were estimated using centrifugation by
449 following a previously described protocol [83]. For dense phase concentration estimation, 100 µl
450 RdRp (10 µM) was incubated at 37 °C for 45 min and centrifuged at ~ 25,000 x g at 37 °C for 15
451 min. After carefully removing the supernatant in several steps, the pure dense phase (~ 2 µL) was
452 re-suspended in 100 µl of the denaturation buffer (6M guanidine hydrochloride, 20 mM sodium
453 phosphate). The absorbance at 280 nm was recorded using nanodrop. The light phase concentration
454 was estimated from the absorbance of the supernatant at 280 nm.

455 **Fluorescence-based activity assay for GII.4 RdRp**

456 GII.4 RdRp activity was measured using a real-time fluorescence-based assay, which uses SYTO9,
457 a fluorescence dye that specifically binds dsRNA but not ssRNA template molecules. Reactions
458 were performed in individual wells of black 96-well flat-bottom plates (costar). The standard
459 reaction contained GII.4 RdRp (5 µM), 20 mM Tris-HCl pH 7.5, 5 mM MgCl2, 2.5 mM MnCl2,
460 40 µg/mL polyC, 5 U RNAseOUT (invitrogen) and 0.25 µM SYTO9 (Sigma-Aldrich). The
461 reaction was initiated by the addition of 300 µM GTP and the fluorescence was recorded after
462 every 2 min over 60 min at 30 °C using a plate reader FlexStation3 (Molecular devices). For
463 measuring the activity of RdRp in the condensates the same reaction was setup in 96 Well glass

464 bottom plates (Cellvis) and the fluorescence was recorded after every 4 min over 60 min at 30 °C
465 using the Yokogawa CV8000 confocal imaging platform.

466 **Thioflavin T fluorescence assays**

467 10 μM GII.4 RdRp was mixed with 10-fold molar excess of ThT and fluorescence intensity was
468 measured using excitation wavelength of 440 nm and emission wavelength of 482 nm using a plate
469 reader FlexStation3 (Molecular devices) at constant temperature of 37 °C and readings were
470 acquired every 2 min with continuous orbital shaking between reads over a period of 24 h. The top
471 of the each well was sealed using adhesive tape to minimize the rate of evaporation. Three
472 independent experiments were performed in triplicates and the bars represent the standard
473 deviation.

474 **Congo red binding assay**

475 CR dye solution was prepared by mixing 7 mg/mL dye in and passed through 0.22 μm filter prior
476 to use. The spectrum of CR (5 μL in 1 mL 20 mM Tris-HCl pH 7.5, 150 mM NaCl and 5 mM
477 DTT) was recorded between 400 and 700 nm at room temperature (negative control). 10 μM RdRp
478 was incubated with C.R. for 12 h at 37 °C and the spectrum were recorded between 400 and 700
479 nm a plate reader FlexStation3 (Molecular devices)

480

481 **Acknowledgments**

482 This research used resources of the Advanced Photon Source, a U.S. Department of Energy (DOE)
483 Office of Science user facility operated for the DOE Office of Science by Argonne National
484 Laboratory under Contract No. DE-AC02-06CH11357. This work was supported by the NIH grant
485 P01 AI057788 and a grant (Q1279) from the Robert Welch Foundation (to BVVP). We also
486 acknowledge Integrated Microscopy Core and the CryoEM Core at Baylor College of Medicine
487 for all the microscopic experiments. We acknowledge the Protein Characterization Unit, Protein

488 and Monoclonal Antibody Production Core, BCM. GK was supported by the Cancer Prevention
489 and Research Institute of Texas grant RR160029 (to Xiaodong Cheng, MD Anderson Cancer
490 Center).

491

492 **References**

493

494 1 Alberti, S. The wisdom of crowds: regulating cell function through condensed states of
495 living matter. *J Cell Sci* **130**, 2789-2796 (2017). https://doi.org:10.1242/jcs.200295
496 2 Banani, S. F., Lee, H. O., Hyman, A. A. & Rosen, M. K. Biomolecular condensates: organizers
497 of cellular biochemistry. *Nat Rev Mol Cell Biol* **18**, 285-298 (2017).
498 https://doi.org:10.1038/nrm.2017.7
499 3 Boeynaems, S. *et al.* Protein Phase Separation: A New Phase in Cell Biology. *Trends Cell*
500 *Biol* **28**, 420-435 (2018). https://doi.org:10.1016/j.tcb.2018.02.004
501 4 Fare, C. M., Villani, A., Drake, L. E. & Shorter, J. Higher-order organization of biomolecular
502 condensates. *Open Biol* **11**, 210137 (2021). https://doi.org:10.1098/rsob.210137
503 5 Brangwynne, C. P. *et al.* Germline P granules are liquid droplets that localize by controlled
504 dissolution/condensation. *Science* **324**, 1729-1732 (2009).
505 https://doi.org:10.1126/science.1172046
506 6 Feric, M. *et al.* Coexisting Liquid Phases Underlie Nucleolar Subcompartments. *Cell* **165**,
507 1686-1697 (2016). https://doi.org:10.1016/j.cell.2016.04.047
508 7 Kaiser, T. E., Intine, R. V. & Dundr, M. De novo formation of a subnuclear body. *Science*
509 **322**, 1713-1717 (2008). https://doi.org:10.1126/science.1165216
510 8 Alberti, S. & Dormann, D. Liquid-Liquid Phase Separation in Disease. *Annu Rev Genet* **53**,
511 171-194 (2019). https://doi.org:10.1146/annurev-genet-112618-043527
512 9 Alberti, S., Gladfelter, A. & Mittag, T. Considerations and Challenges in Studying Liquid-
513 Liquid Phase Separation and Biomolecular Condensates. *Cell* **176**, 419-434 (2019).
514 https://doi.org:10.1016/j.cell.2018.12.035
515 10 Alberti, S. & Hyman, A. A. Biomolecular condensates at the nexus of cellular stress, protein
516 aggregation disease and ageing. *Nat Rev Mol Cell Biol* **22**, 196-213 (2021).
517 https://doi.org:10.1038/s41580-020-00326-6
518 11 Fuxreiter, M. & Vendruscolo, M. Generic nature of the condensed states of proteins. *Nat*
519 *Cell Biol* **23**, 587-594 (2021). https://doi.org:10.1038/s41556-021-00697-8
520 12 Hardenberg, M., Horvath, A., Ambrus, V., Fuxreiter, M. & Vendruscolo, M. Widespread
521 occurrence of the droplet state of proteins in the human proteome. *Proc Natl Acad Sci U*
522 *S A* **117**, 33254-33262 (2020). https://doi.org:10.1073/pnas.2007670117
523 13 Shin, Y. & Brangwynne, C. P. Liquid phase condensation in cell physiology and disease.
524 *Science* **357** (2017). https://doi.org:10.1126/science.aaf4382
525 14 Peng, P. H., Hsu, K. W. & Wu, K. J. Liquid-liquid phase separation (LLPS) in cellular
526 physiology and tumor biology. *Am J Cancer Res* **11**, 3766-3776 (2021).

527 15 Zhang, H. *et al.* Liquid-liquid phase separation in biology: mechanisms, physiological
528 functions and human diseases. *Sci China Life Sci* **63**, 953-985 (2020).
529 https://doi.org:10.1007/s11427-020-1702-x
530 16 Kroschwald, S. *et al.* Promiscuous interactions and protein disaggregases determine the
531 material state of stress-inducible RNP granules. *Elife* **4**, e06807 (2015).
532 https://doi.org:10.7554/eLife.06807
533 17 Jain, S. *et al.* ATPase-Modulated Stress Granules Contain a Diverse Proteome and
534 Substructure. *Cell* **164**, 487-498 (2016). https://doi.org:10.1016/j.cell.2015.12.038
535 18 Martin, E. W. & Mittag, T. Relationship of Sequence and Phase Separation in Protein Low-
536 Complexity Regions. *Biochemistry* **57**, 2478-2487 (2018).
537 https://doi.org:10.1021/acs.biochem.8b00008
538 19 Hughes, M. P. *et al.* Atomic structures of low-complexity protein segments reveal kinked
539 beta sheets that assemble networks. *Science* **359**, 698-701 (2018).
540 https://doi.org:10.1126/science.aan6398
541 20 Maharana, S. *et al.* RNA buffers the phase separation behavior of prion-like RNA binding
542 proteins. *Science* **360**, 918-921 (2018). https://doi.org:10.1126/science.aar7366
543 21 Pak, C. W. *et al.* Sequence Determinants of Intracellular Phase Separation by Complex
544 Coacervation of a Disordered Protein. *Mol Cell* **63**, 72-85 (2016).
545 https://doi.org:10.1016/j.molcel.2016.05.042
546 22 Choi, J. M., Holehouse, A. S. & Pappu, R. V. Physical Principles Underlying the Complex
547 Biology of Intracellular Phase Transitions. *Annu Rev Biophys* **49**, 107-133 (2020).
548 https://doi.org:10.1146/annurev-biophys-121219-081629
549 23 Uversky, V. N. Intrinsically disordered proteins in overcrowded milieu: Membrane-less
550 organelles, phase separation, and intrinsic disorder. *Curr Opin Struct Biol* **44**, 18-30 (2017).
551 https://doi.org:10.1016/j.sbi.2016.10.015
552 24 Hyman, A. A., Weber, C. A. & Julicher, F. Liquid-liquid phase separation in biology. *Annu*
553 *Rev Cell Dev Biol* **30**, 39-58 (2014). https://doi.org:10.1146/annurev-cellbio-100913-
554 013325
555 25 Wei, M. T. *et al.* Phase behaviour of disordered proteins underlying low density and high
556 permeability of liquid organelles. *Nat Chem* **9**, 1118-1125 (2017).
557 https://doi.org:10.1038/nchem.2803
558 26 Geiger, F. *et al.* Liquid-liquid phase separation underpins the formation of replication
559 factories in rotaviruses. *EMBO J* **40**, e107711 (2021).
560 https://doi.org:10.15252/embj.2021107711
561 27 Wang, J., Shi, C., Xu, Q. & Yin, H. SARS-CoV-2 nucleocapsid protein undergoes liquid-liquid
562 phase separation into stress granules through its N-terminal intrinsically disordered
563 region. *Cell Discov* **7**, 5 (2021). https://doi.org:10.1038/s41421-020-00240-3
564 28 Savastano, A., Ibanez de Opakua, A., Rankovic, M. & Zweckstetter, M. Nucleocapsid
565 protein of SARS-CoV-2 phase separates into RNA-rich polymerase-containing
566 condensates. *Nat Commun* **11**, 6041 (2020). https://doi.org:10.1038/s41467-020-19843-
567 1
568 29 Rahman, S. K., Ampah, K. K. & Roy, P. Role of NS2 specific RNA binding and
569 phosphorylation in liquid-liquid phase separation and virus assembly. *Nucleic Acids Res*
570 **50**, 11273-11284 (2022). https://doi.org:10.1093/nar/gkac904

30 Brocca, S., Grandori, R., Longhi, S. & Uversky, V. Liquid-Liquid Phase Separation by Intrinsically Disordered Protein Regions of Viruses: Roles in Viral Life Cycle and Control of Virus-Host Interactions. *Int J Mol Sci* **21** (2020). https://doi.org:10.3390/ijms21239045

31 Reddy, V. *et al.* Birnaviridae Virus Factories Show Features of Liquid-Liquid Phase Separation and Are Distinct from Paracrystalline Arrays of Virions Observed by Electron Microscopy. *J Virol* **96**, e0202421 (2022). https://doi.org:10.1128/jvi.02024-21

32 Chau, B. A., Chen, V., Cochrane, A. W., Parent, L. J. & Mouland, A. J. Liquid-liquid phase separation of nucleocapsid proteins during SARS-CoV-2 and HIV-1 replication. *Cell Rep* **42**, 111968 (2022). https://doi.org:10.1016/j.celrep.2022.111968

33 Wang, S. *et al.* Targeting liquid-liquid phase separation of SARS-CoV-2 nucleocapsid protein promotes innate antiviral immunity by elevating MAVS activity. *Nat Cell Biol* **23**, 718-732 (2021). https://doi.org:10.1038/s41556-021-00710-0

34 Wei, W. *et al.* When liquid-liquid phase separation meets viral infections. *Front Immunol* **13**, 985622 (2022). https://doi.org:10.3389/fimmu.2022.985622

35 Kirk, M. D. *et al.* World Health Organization Estimates of the Global and Regional Disease Burden of 22 Foodborne Bacterial, Protozoal, and Viral Diseases, 2010: A Data Synthesis. *PLoS Med* **12**, e1001921 (2015). https://doi.org:10.1371/journal.pmed.1001921

36 Mortality, G. B. D. & Causes of Death, C. Global, regional, and national age-sex specific all-cause and cause-specific mortality for 240 causes of death, 1990-2013: a systematic analysis for the Global Burden of Disease Study 2013. *Lancet* **385**, 117-171 (2015). https://doi.org:10.1016/S0140-6736(14)61682-2

37 Bartsch, S. M., Lopman, B. A., Ozawa, S., Hall, A. J. & Lee, B. Y. Global Economic Burden of Norovirus Gastroenteritis. *PLoS One* **11**, e0151219 (2016). https://doi.org:10.1371/journal.pone.0151219

38 Mattison, C. P., Cardemil, C. V. & Hall, A. J. Progress on norovirus vaccine research: public health considerations and future directions. *Expert Rev Vaccines* **17**, 773-784 (2018). https://doi.org:10.1080/14760584.2018.1510327

39 Lopman, B. A., Steele, D., Kirkwood, C. D. & Parashar, U. D. The Vast and Varied Global Burden of Norovirus: Prospects for Prevention and Control. *PLoS Med* **13**, e1001999 (2016). https://doi.org:10.1371/journal.pmed.1001999

40 Chhabra, P. *et al.* Updated classification of norovirus genogroups and genotypes. *J Gen Virol* **100**, 1393-1406 (2019). https://doi.org:10.1099/jgv.0.001318

41 van Beek, J. *et al.* Molecular surveillance of norovirus, 2005-16: an epidemiological analysis of data collected from the NoroNet network. *Lancet Infect Dis* **18**, 545-553 (2018). https://doi.org:10.1016/S1473-3099(18)30059-8

42 Yang, Y. *et al.* Genetic and phenotypic characterization of GII-4 noroviruses that circulated during 1987 to 2008. *J Virol* **84**, 9595-9607 (2010). https://doi.org:10.1128/JVI.02614-09

43 Campillay-Veliz, C. P. *et al.* Human Norovirus Proteins: Implications in the Replicative Cycle, Pathogenesis, and the Host Immune Response. *Front Immunol* **11**, 961 (2020). https://doi.org:10.3389/fimmu.2020.00961

44 Vongpunsawad, S., Venkataram Prasad, B. V. & Estes, M. K. Norwalk Virus Minor Capsid Protein VP2 Associates within the VP1 Shell Domain. *J Virol* **87**, 4818-4825 (2013). https://doi.org:10.1128/JVI.03508-12

614 45 Ayyar, B. V. *et al.* CLIC and membrane wound repair pathways enable pandemic norovirus
615 entry and infection. *Nat Commun* **14**, 1148 (2023). https://doi.org:10.1038/s41467-023-
616 36398-z
617 46 Ettayebi, K. *et al.* Replication of human noroviruses in stem cell-derived human enteroids.
618 *Science* **353**, 1387-1393 (2016). https://doi.org:10.1126/science.aaf5211
619 47 Alvarado, G. *et al.* Broadly cross-reactive human antibodies that inhibit genogroup I and
620 II noroviruses. *Nat Commun* **12**, 4320 (2021). https://doi.org:10.1038/s41467-021-24649-
621 w
622 48 Saar, K. L. *et al.* Learning the molecular grammar of protein condensates from sequence
623 determinants and embeddings. *Proc Natl Acad Sci U S A* **118** (2021).
624 https://doi.org:10.1073/pnas.2019053118
625 49 Xue, B., Dunbrack, R. L., Williams, R. W., Dunker, A. K. & Uversky, V. N. PONDR-FIT: a meta-
626 predictor of intrinsically disordered amino acids. *Biochim Biophys Acta* **1804**, 996-1010
627 (2010). https://doi.org:10.1016/j.bbapap.2010.01.011
628 50 Dosztanyi, Z. Prediction of protein disorder based on IUPred. *Protein Sci* **27**, 331-340
629 (2018). https://doi.org:10.1002/pro.3334
630 51 Deval, J., Jin, Z., Chuang, Y. C. & Kao, C. C. Structure(s), function(s), and inhibition of the
631 RNA-dependent RNA polymerase of noroviruses. *Virus Res* **234**, 21-33 (2017).
632 https://doi.org:10.1016/j.virusres.2016.12.018
633 52 Lee, J. H. *et al.* Insight Into the Interaction Between RNA Polymerase and VPg for Murine
634 Norovirus Replication. *Front Microbiol* **9**, 1466 (2018).
635 https://doi.org:10.3389/fmicb.2018.01466
636 53 Shaik, M. M., Bhattacharjee, N., Feliks, M., Ng, K. K. & Field, M. J. Norovirus RNA-
637 dependent RNA polymerase: A computational study of metal-binding preferences.
638 *Proteins* **85**, 1435-1445 (2017). https://doi.org:10.1002/prot.25304
639 54 Smertina, E., Urakova, N., Strive, T. & Frese, M. Calicivirus RNA-Dependent RNA
640 Polymerases: Evolution, Structure, Protein Dynamics, and Function. *Front Microbiol* **10**,
641 1280 (2019). https://doi.org:10.3389/fmicb.2019.01280
642 55 Batishchev, O. V. *et al.* pH-Dependent Formation and Disintegration of the Influenza A
643 Virus Protein Scaffold To Provide Tension for Membrane Fusion. *J Virol* **90**, 575-585
644 (2016). https://doi.org:10.1128/JVI.01539-15
645 56 Liu, H., Maruyama, H., Masuda, T., Honda, A. & Arai, F. The Influence of Virus Infection on
646 the Extracellular pH of the Host Cell Detected on Cell Membrane. *Front Microbiol* **7**, 1127
647 (2016). https://doi.org:10.3389/fmicb.2016.01127
648 57 Jimenez, L. *et al.* Acid pH Increases SARS-CoV-2 Infection and the Risk of Death by COVID-
649 19. *Front Med (Lausanne)* **8**, 637885 (2021). https://doi.org:10.3389/fmed.2021.637885
650 58 Kreutzberger, A. J. B. *et al.* SARS-CoV-2 requires acidic pH to infect cells. *Proc Natl Acad*
651 *Sci U S A* **119**, e2209514119 (2022). https://doi.org:10.1073/pnas.2209514119
652 59 Rohayem, J., Robel, I., Jager, K., Scheffler, U. & Rudolph, W. Protein-primed and de novo
653 initiation of RNA synthesis by norovirus 3Dpol. *J Virol* **80**, 7060-7069 (2006).
654 https://doi.org:10.1128/JVI.02195-05
655 60 Belliot, G., Sosnovtsev, S. V., Chang, K. O., McPhie, P. & Green, K. Y. Nucleotidylylation of
656 the VPg protein of a human norovirus by its proteinase-polymerase precursor protein.
657 *Virology* **374**, 33-49 (2008). https://doi.org:10.1016/j.virol.2007.12.028

658 61 Hyde, J. L. *et al.* Mouse norovirus replication is associated with virus-induced vesicle
659 clusters originating from membranes derived from the secretory pathway. *J Virol* **83**,
660 9709-9719 (2009). https://doi.org:10.1128/JVI.00600-09
661 62 Palacio, M. & Taatjes, D. J. Merging Established Mechanisms with New Insights:
662 Condensates, Hubs, and the Regulation of RNA Polymerase II Transcription. *J Mol Biol* **434**,
663 167216 (2022). https://doi.org:10.1016/j.jmb.2021.167216
664 63 Ladouceur, A. M. *et al.* Clusters of bacterial RNA polymerase are biomolecular
665 condensates that assemble through liquid-liquid phase separation. *Proc Natl Acad Sci U S*
666 *A* **117**, 18540-18549 (2020). https://doi.org:10.1073/pnas.2005019117
667 64 Murakami, K. *et al.* Bile acids and ceramide overcome the entry restriction for GII.3 human
668 norovirus replication in human intestinal enteroids. *Proc Natl Acad Sci U S A* **117**, 1700-
669 1710 (2020). https://doi.org:10.1073/pnas.1910138117
670 65 Perdikari, T. M. *et al.* SARS-CoV-2 nucleocapsid protein undergoes liquid-liquid phase
671 separation stimulated by RNA and partitions into phases of human ribonucleoproteins.
672 *bioRxiv* (2020). https://doi.org:10.1101/2020.06.09.141101
673 66 Fang, J. *et al.* Spatial and functional arrangement of Ebola virus polymerase inside phase-
674 separated viral factories. *Nat Commun* **14**, 4159 (2023). https://doi.org:10.1038/s41467-
675 023-39821-7
676 67 Li, T. F. *et al.* Human Norovirus NS3 Has RNA Helicase and Chaperoning Activities. *J Virol*
677 **92** (2018). https://doi.org:10.1128/JVI.01606-17
678 68 Harak, C. & Lohmann, V. Ultrastructure of the replication sites of positive-strand RNA
679 viruses. *Virology* **479-480**, 418-433 (2015). https://doi.org:10.1016/j.virol.2015.02.029
680 69 Zhang, Y., Cao, X. & Li, D. Architecture of viral replication factories. *Oncotarget* **6**, 30439-
681 30440 (2015). https://doi.org:10.18632/oncotarget.5900
682 70 Zhang, Z. *et al.* Host Lipids in Positive-Strand RNA Virus Genome Replication. *Front*
683 *Microbiol* **10**, 286 (2019). https://doi.org:10.3389/fmicb.2019.00286
684 71 Ditlev, J. A. Membrane-associated phase separation: organization and function emerge
685 from a two-dimensional milieu. *J Mol Cell Biol* **13**, 319-324 (2021).
686 https://doi.org:10.1093/jmcb/mjab010
687 72 Miller, E. J. *et al.* Divide and conquer: How phase separation contributes to lateral
688 transport and organization of membrane proteins and lipids. *Chem Phys Lipids* **233**,
689 104985 (2020). https://doi.org:10.1016/j.chemphyslip.2020.104985
690 73 Lyle, J. M., Bullitt, E., Bienz, K. & Kirkegaard, K. Visualization and functional analysis of
691 RNA-dependent RNA polymerase lattices. *Science* **296**, 2218-2222 (2002).
692 https://doi.org:10.1126/science.1070585
693 74 Bentham, M., Holmes, K., Forrest, S., Rowlands, D. J. & Stonehouse, N. J. Formation of
694 higher-order foot-and-mouth disease virus 3D(pol) complexes is dependent on elongation
695 activity. *J Virol* **86**, 2371-2374 (2012). https://doi.org:10.1128/JVI.05696-11
696 75 Loundras, E. A. *et al.* Higher-order structures of the foot-and-mouth disease virus RNA-
697 dependent RNA polymerase required for genome replication. *Commun Biol* **5**, 61 (2022).
698 https://doi.org:10.1038/s42003-021-02989-z
699 76 Bhardwaj, T. *et al.* Amyloidogenic proteins in the SARS-CoV and SARS-CoV-2 proteomes.
700 *Nat Commun* **14**, 945 (2023). https://doi.org:10.1038/s41467-023-36234-4

701 77 Schuck, P., Perugini, M. A., Gonzales, N. R., Howlett, G. J. & Schubert, D. Size-distribution
702 analysis of proteins by analytical ultracentrifugation: strategies and application to model
703 systems. *Biophys J* **82**, 1096-1111 (2002). https://doi.org:10.1016/S0006-3495(02)75469-
704 6
705 78 Laue TM, S. B., Ridgeway TM., Pelletier SL. Computer-aided Interpretation of
706 Sedimentation Data for Proteins. *Analytical ultracentrifugation in biochemistry and*
707 *polymer science*, pp. 90–25 (1992).
708 79 Winn, M. D. *et al.* Overview of the CCP4 suite and current developments. *Acta Crystallogr*
709 *D Biol Crystallogr* **67**, 235-242 (2011). https://doi.org:10.1107/S0907444910045749
710 80 Adams, P. D. *et al.* PHENIX: a comprehensive Python-based system for macromolecular
711 structure solution. *Acta Crystallogr D Biol Crystallogr* **66**, 213-221 (2010).
712 https://doi.org:10.1107/S0907444909052925
713 81 Emsley, P., Lohkamp, B., Scott, W. G. & Cowtan, K. Features and development of Coot.
714 *Acta Crystallogr D Biol Crystallogr* **66**, 486-501 (2010).
715 https://doi.org:10.1107/S0907444910007493
716 82 Karandikar, U. C. *et al.* Detection of human norovirus in intestinal biopsies from
717 immunocompromised transplant patients. *J Gen Virol* **97**, 2291-2300 (2016).
718 https://doi.org:10.1099/jgv.0.000545
719 83 Milkovic, N. M. & Mittag, T. Determination of Protein Phase Diagrams by Centrifugation.
720 *Methods Mol Biol* **2141**, 685-702 (2020). https://doi.org:10.1007/978-1-0716-0524-0_35
721

722

723 **Figures and legends**

724

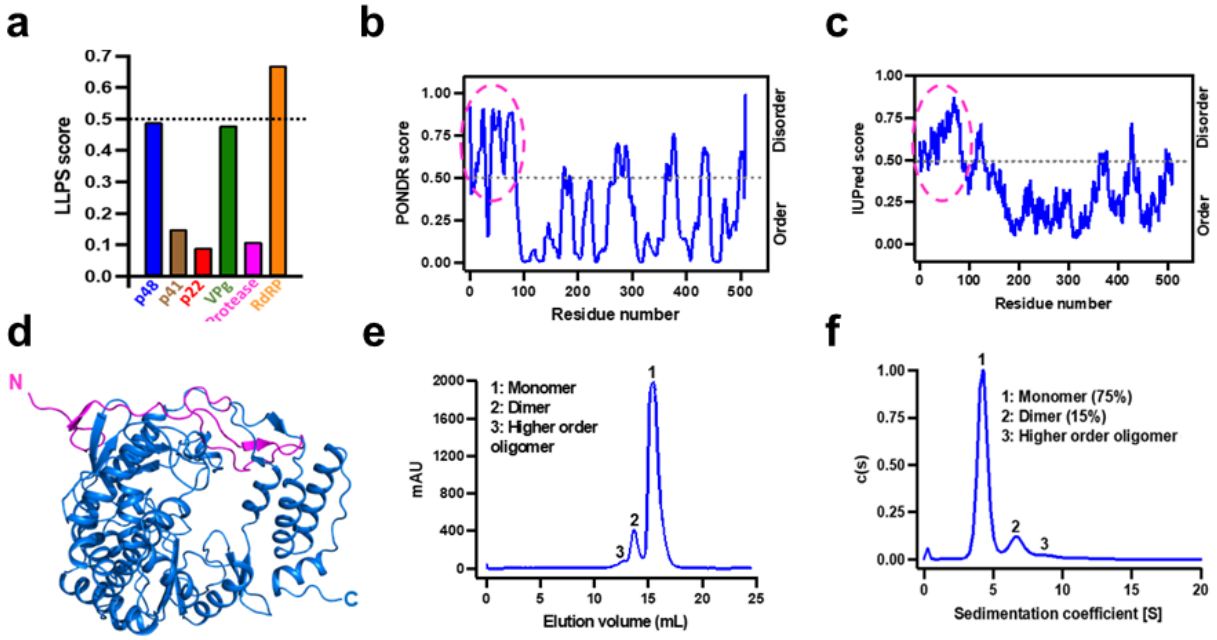

725
726

727 **Figure 1. GII.4 RdRp has the required properties to undergo LLPS**. **(a)** Bioinformatics
728 analysis of the primary amino acid sequences of all nonstructural proteins of HuNoV GII.4 to
729 predict LLPS propensity using DeePhase. The dotted black line indicates the threshold LLPS score
730 of proteins to undergo LLPS. **(b-c)** The disorder prediction of GII.4 RdRp primary amino acid
731 sequence using bioinformatics tools **(b)** PONDR **(c)** IUPred2. The dotted black line in both the
732 panels indicates the threshold disorder score. The dotted pink circle in both the panels shows the
733 predicted disordered N-terminal region. (**d)** The cartoon representation of the crystal structure of
734 GII.4 RdRp showing the disordered N-terminal region colored in pink. **(e-f)** The oligomeric state
735 of GII.4 RdRp analyzed using **(e)** size exclusion chromatography and **(f)** sedimentation velocity
736 analytical ultracentrifugation.

737

738

739

740

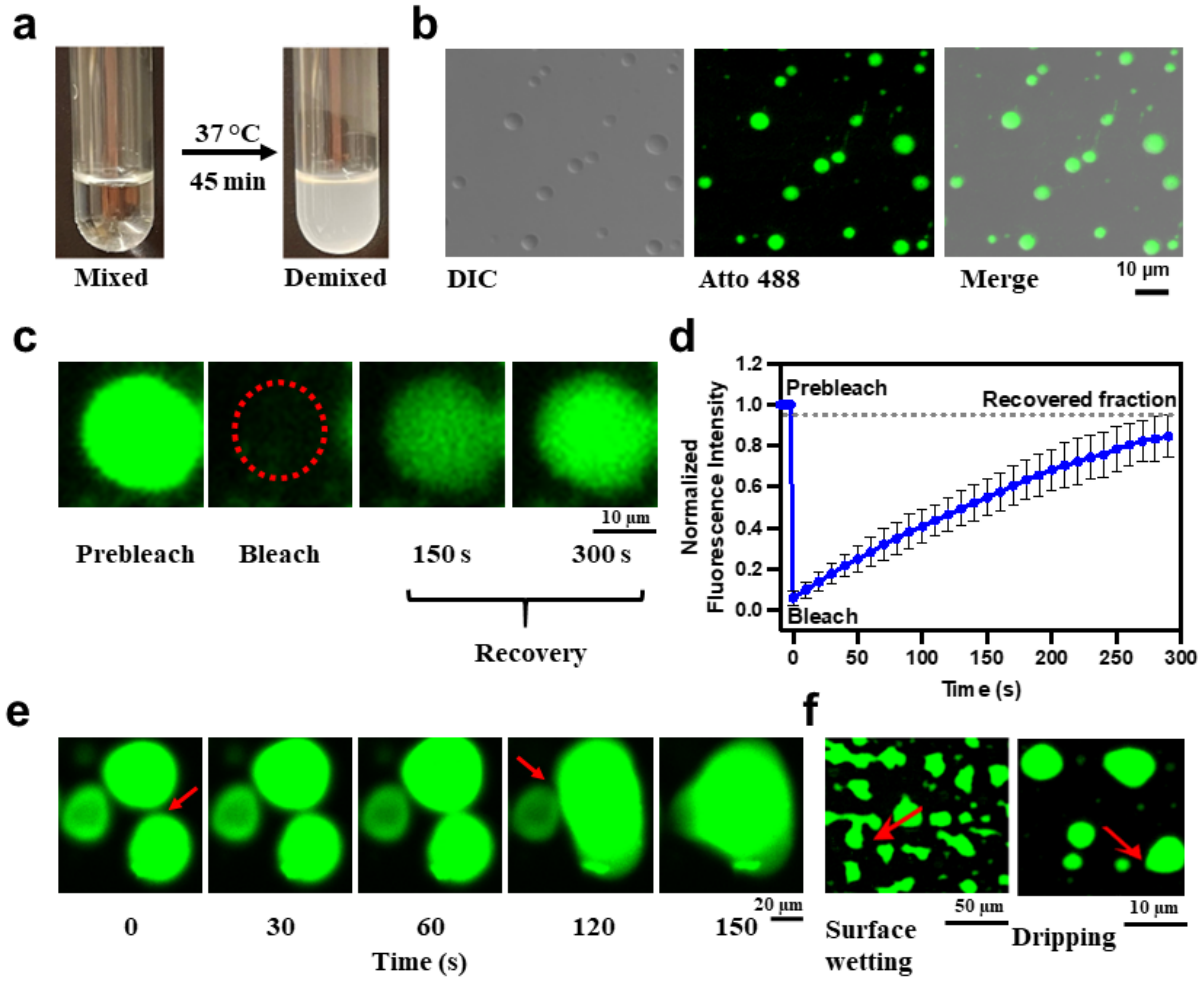

741
742
743 **Figure 2. GII.4 RdRp undergoes LLPS in vitro. (a)** Phase separation of RdRp from a
744 homogeneous mixed-phase into a demixed phase upon incubation at 37 °C for 45 min. **(b)**
745 Differential interference contrast (DIC) and confocal images of phase separated RdRp (1 % Atto
746 488 labeled and 99 % unlabeled). Phase separated GII.4 RdRp possesses liquid-like properties. **(c)**
747 FRAP of RdRp in condensate photobleached at the position indicated by the red circle. **(d)** The
748 graph shows the recovery curve where normalized fluorescence intensity was plotted against time.
749 **(e)** Time-lapse images of RdRp condensates exhibits formation of larger condensate by fusion of
750 smaller condensates over time. The red arrows indicate the site of fusion. **(f)** Surface wetting and
751 dripping using confocal microscopy. The red arrows indicate the position of surface wetting and
752 dripping.
753
754

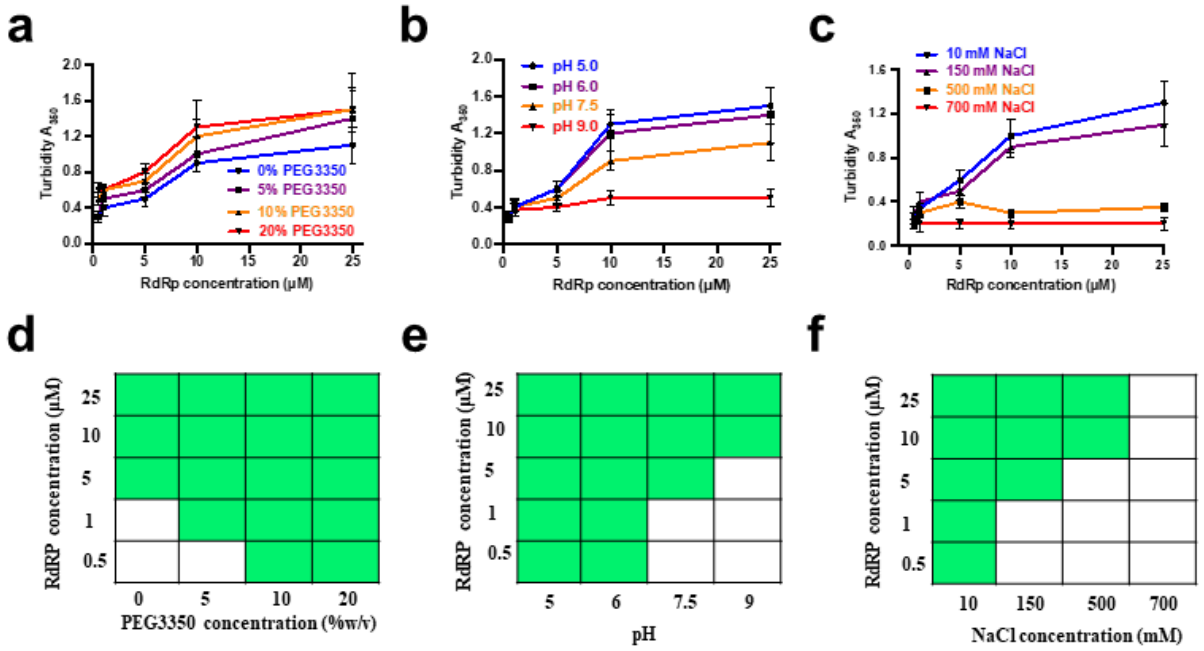

Figure 3. Phase separation of GII.4 RdRp is modulated by PEG3350 concentration, pH, and salt concentration. Effect of **(a)** protein and PEG3350 concentrations, **(b)** protein concentrations and pH, **(c)** protein and salt concentrations on the phase separation of RdRp was assessed by measuring the turbidity of the samples at OD 350 nm. **(d-f)** A phase diagram of RdRp at **(d)** protein and PEG3350 concentrations, **(e)** at protein concentrations and pH, at **(f)** protein and salt concentrations constructed from the confocal microscopy images. The green boxes indicate LLPS (condensate state) and white boxes indicate no LLPS (soluble state).

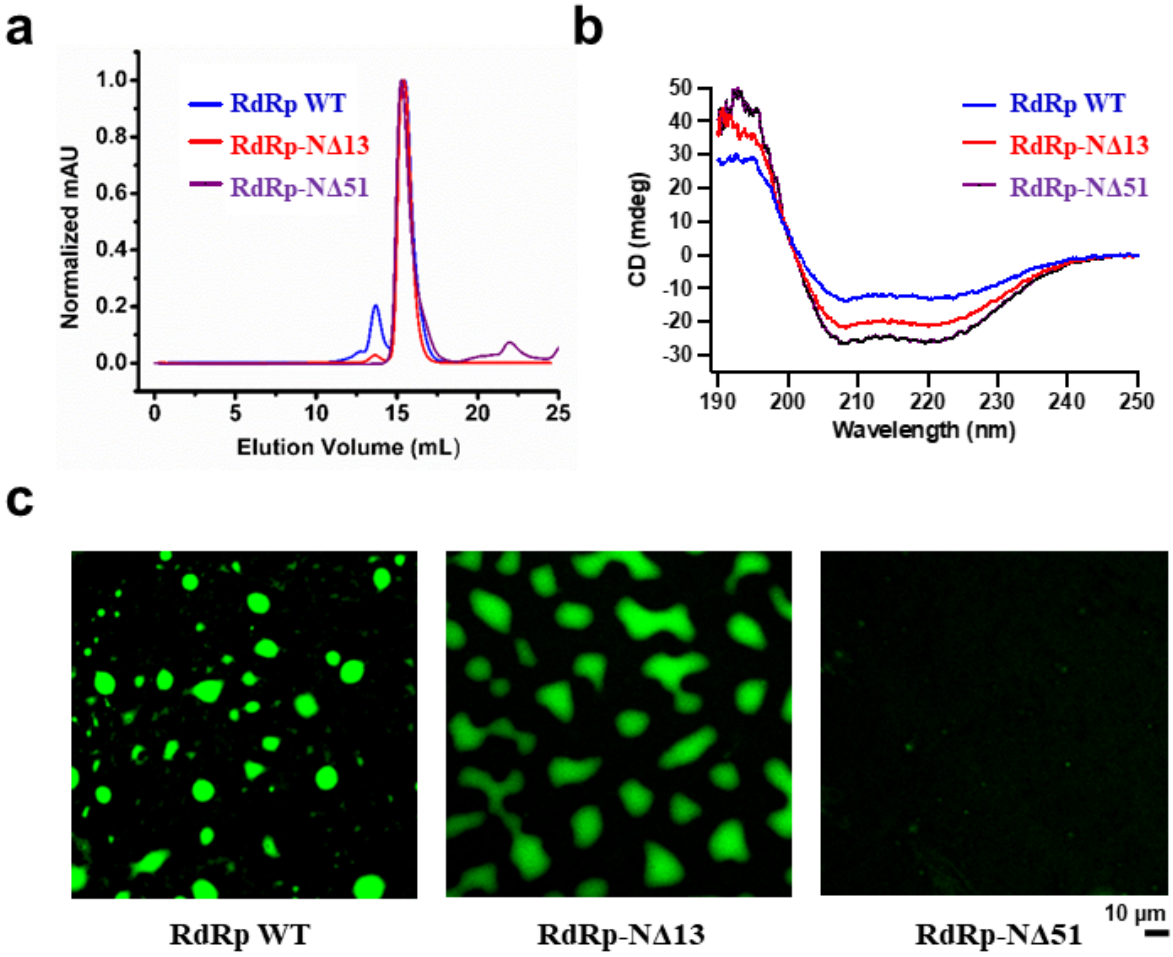

775

776 **Figure 4. Effect of N-terminal deletion on phase separation of GII.4 RdRp.** RdRp WT, RdRp-
777 NΔ13, and RdRp-NΔ51 were analyzed by **(a)** The size exclusion chromatography profile **(b)** CD
778 spectroscopy profile and **(c)** confocal microscopy.

779

780

781

782

783

784

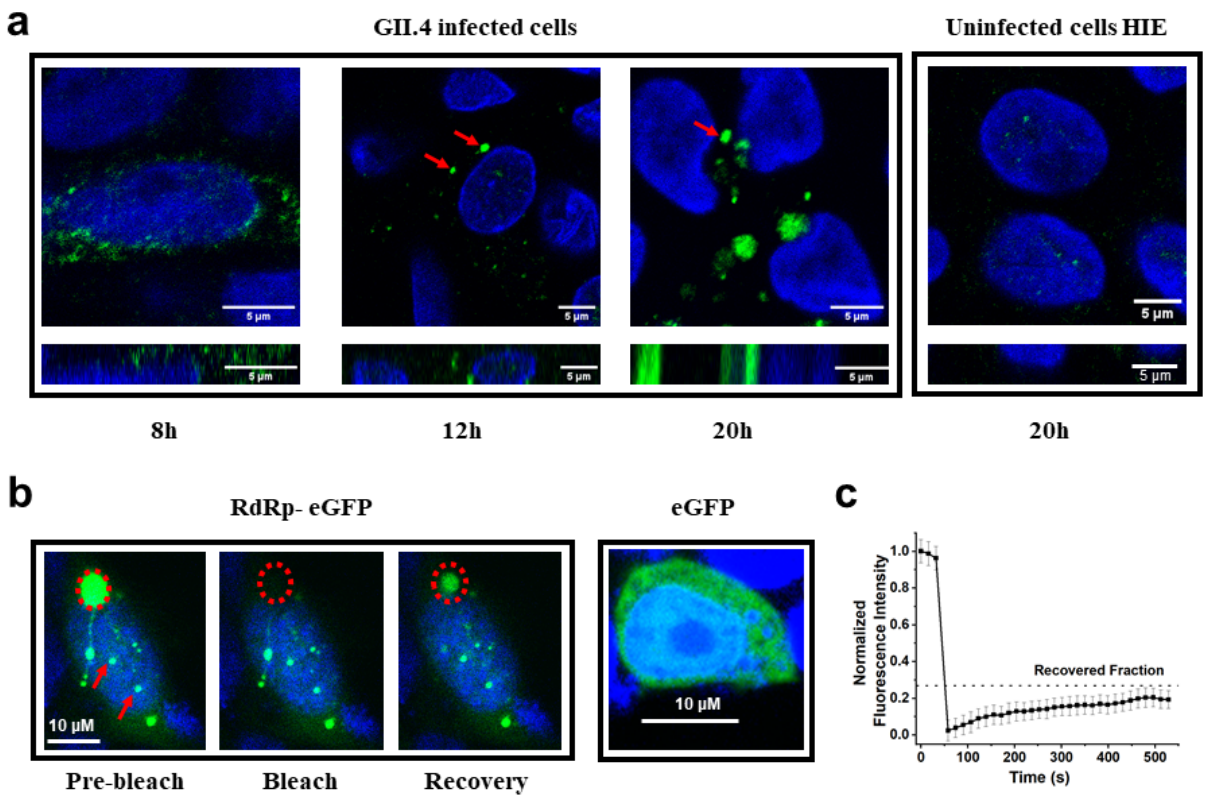

Figure 5. RdRp forms condensates in GII.4 infected HIEs. (a) Confocal microscopy images of GII.4 HuNoV-infected HIEs at different time points post infection showing condensate formation detected by anti-RdRp antibody (green). Uninfected HIEs were used as negative control. Red arrows indicate the position of representative condensates. **(b)** Transfection of RdRp-eGFP in HEK293T cells showing condensate formation (red arrows). FRAP experiment was performed on one of the condensates (marked by red circle) which shows recovery of the RdRp molecules. The eGFP transfected HEK293T cells were used as a negative control where GFP is diffuse. **(c)** Recovery curve of normalized fluorescence intensity was plotted against time for FRAP experiment.

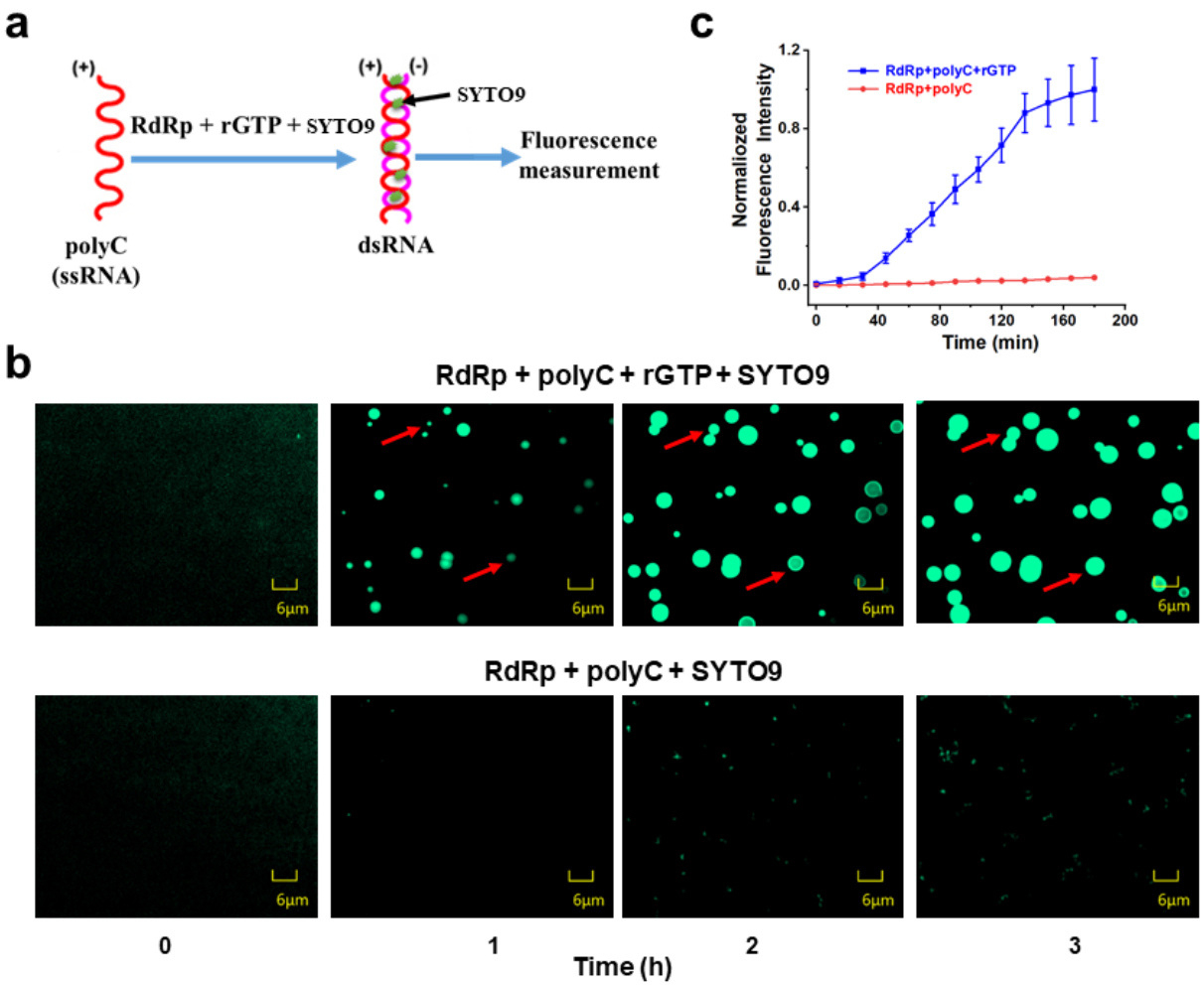

Figure 6. GII.4 RdRp is enzymatically active in the condensates. (a) A schematic representation of the assay to detect the formation of dsRNA from ssRNA by RdRp using SYTO9 dye. **(b)** Microscopic images of time-dependent activity of RdRp measured by fluorescence intensity of SYTO9: the upper panel contains all the components of reaction mixture. A time-dependent increase in the fluorescence intensity of SYTO9 which is an indicative of dsRNA formation within the condensates was observed. The red arrows indicate representative condensates showing an increase in fluorescence intensity over time. The lower panel without rGTP in reaction mixture serves as a negative control. **(c)** The graph of normalized fluorescence intensity plotted against time shows an overall increase in fluorescence intensity.

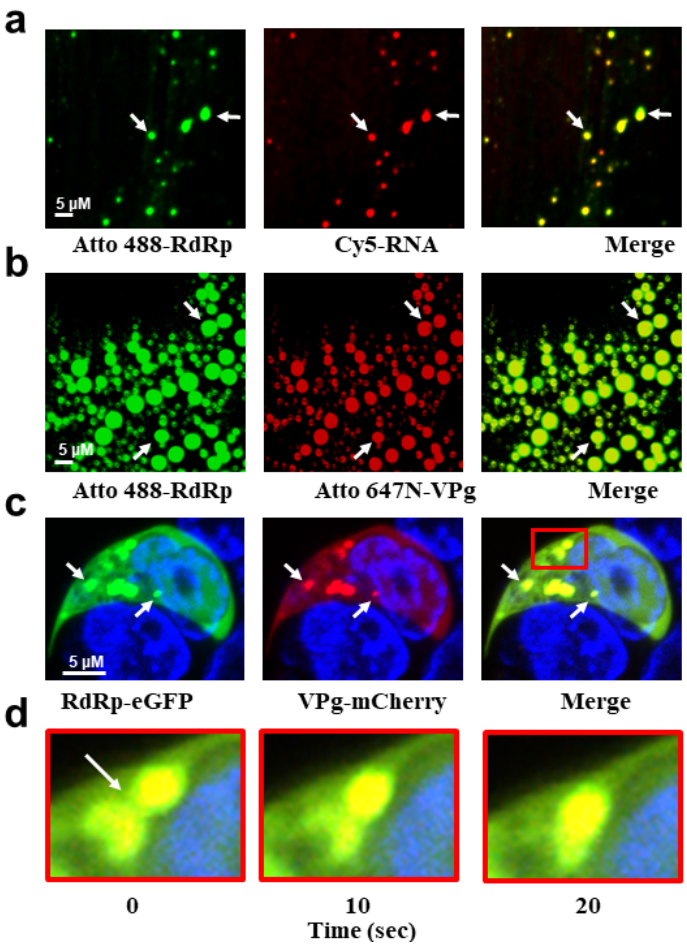

Figure 7. GII.4 RdRp condensates sequester components of viral replication machinery Confocal images showing the recruitment of **(a)** Cy5-RNA and **(b)** Atto 647N-VPg into the spherical condensates formed by Atto 488-RdRp. **(c)** Colocalization (yellow) of mCherry-VPg (red) and GII.4 RdRp-eGFP (green) was seen on overexpression of these protein in HEK293T cells. In the above panels, the white arrows indicate the position of representative condensates and their co-localization with the components of replication machinery. **(d)** Time lapse images of site indicated by red box in panel C showing the fusion of condensates. The white arrow indicates the position of fusion.

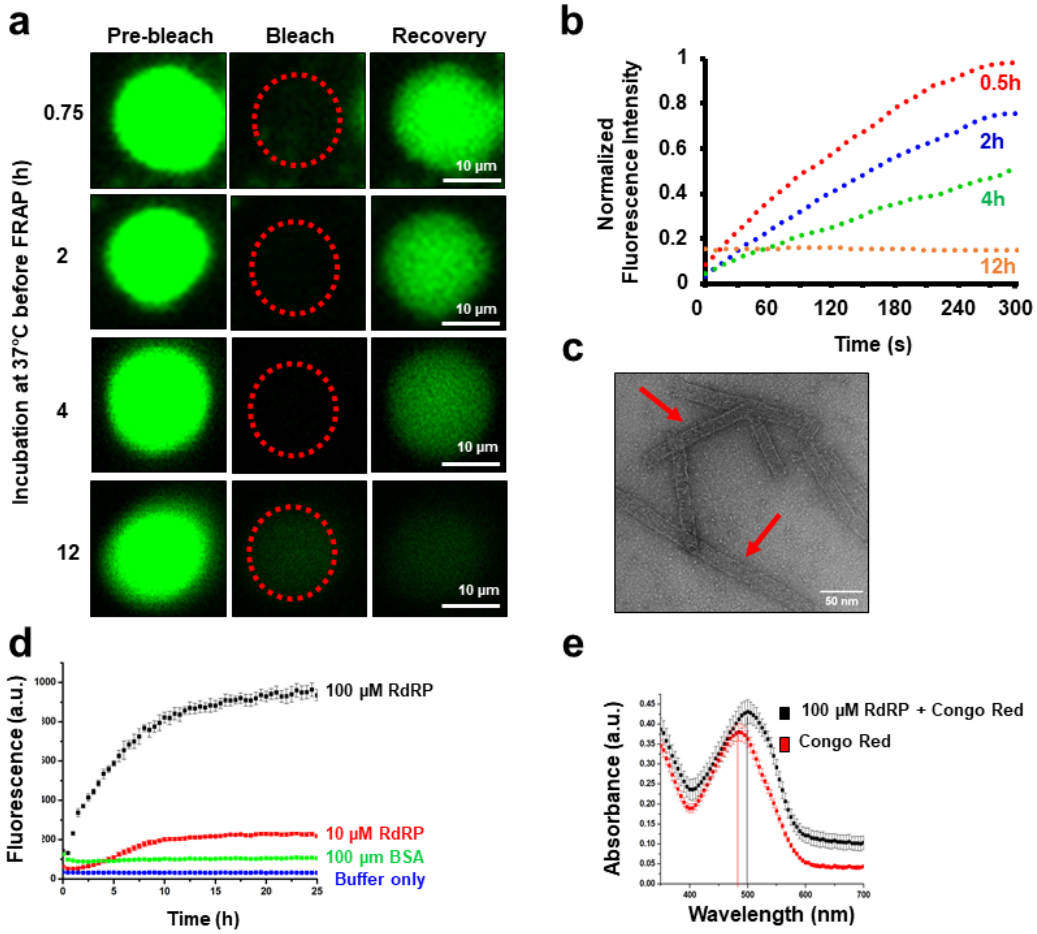

Figure 8. The dynamics of GII.4 RdRp slow down with time in the droplet and leads to the formation of amyloid fibrils (a) FRAP of condensates incubated at 37 °C for indicated time points to measure the dynamics of RdRp molecules in the condensates. **(b)** The recovery graph of the FRAP experiments performed in panel A. The results indicate a slowdown in the dynamics of RdRp molecules over time. **(c)** Negative staining image of RdRp incubated at 37 °C for 12 h. The red arrows indicate the positions of fibrils. **(d)** The kinetics of amyloid fibril formation of RdRp was monitored at 37 °C using ThT fluorescence assay. **(e)** CR absorbance spectra in the absence and presence of RdRp suggests a red shift in the absorbance maxima of CR in the presence of RdRp.

Supplementary Table 1: **Data collection and refinement statistics**

	GII.4 RdRp
Data collection	
Space group	$P2_12_12_1$
Cell dimensions	
a, *b*, *c* (Å)	83.07, 83.70, 90.72
α, β, γ (°)	90. 90, 90
Resolution (Å)	37.21-2.03(2.10-2.03) *
Wavelength (Å)	1.0
R_{sym} or R_{merge}	0.27(7.5)
I / σI	8.4(0.8l)
Completeness (%)	99.86(99.27)
Redundancy	11.4(10.5)
Refinement	
Resolution (Å)	2.03
No. reflections	41484
R_{work} / R_{free}	0.21/0.24
No. atoms	
Protein	3991
Ligand/ion	33
Water	158
B-factors (Å^2)	
Protein	44.09
Ligand/ion	56.32
Water	47.07
R.M.S. deviations	
Bond lengths (Å)	0.005
Bond angles (°)	0.67

*Values in parentheses are for the highest resolution shell.

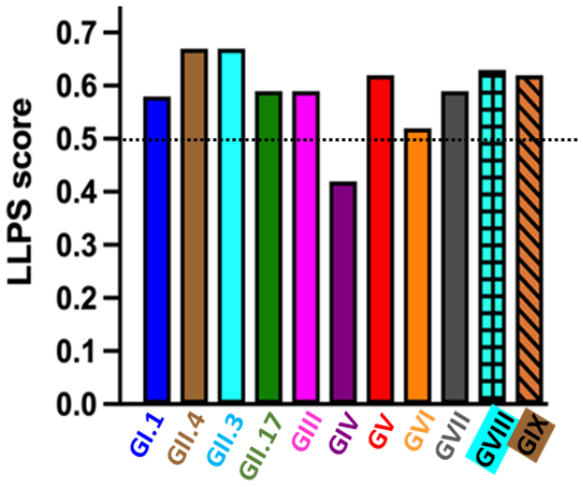

Supplementary Figure 1. RdRp of norovirus genogroups has the propensity to form LLPS. Bioinformatics analysis of the primary amino acid sequences of RdRp of different norovirus genogroups using DeePhase to predict LLPS propensity. The dotted black line indicates the threshold LLPS score of proteins to undergo LLPS.